Post Fault Operation of a Bearingless Multi-Sector SPM Machine by Space Vector Control

(Article begins on next page)

31 October 2024

This is the final peer-reviewed accepted manuscript of:

Terms of use:

Post Fault Operation of Bearingless Multi-Sector SPM Machines by Space Vector Control

Giacomo Sala, Giorgio Valente, *Member IEEE*, David Gerada, Pericle Zanchetta, *Senior Member IEEE*, and Chris Gerada, *Senior Member IEEE*

Abstract—In this paper a novel post fault control algorithm based on the space vector method is presented and applied to a bearingless multi-sector permanent magnet synchronous machine with a triple three-phase winding.

Firstly, the expressions of the current space vectors as a function of the electromagnetic suspension force and motoring torque are introduced. Then, the open-circuit fault is described and a new post fault algorithm is introduced.

The introduced post fault algorithm, based on the minimization of the stator copper losses, is compared at simulation level with an existing one, where the above-mentioned loss minimization was not considered. The simulation results show a remarkable improvement in the performance when the novel post fault algorithm is employed. Finally, the developed control algorithm is experimentally validated on a prototype of a bearingless multi-sector permanent magnet synchronous machine.

Index Terms—Bearingless machines, Open-circuit faults, Fault tolerant control, Force control, Machine vector control, Magnetic levitation, Multiphase machines, Permanent magnet machines.

List of Acronims

PM	Permanent Magnet.
MS-SPM	Multi-Sector Surface Permanent Magnet.
BM	Bearingless Machine.
SV	Space Vector.
VSI	Voltage Source Inverter.
PFC	Post Fault Control.
DoF	Degree of Freedom.

I. Introduction

BEARINGLESS Machines (BM) are relatively recent electromagnetic devices that allow to simultaneously generate suspension force and motoring torque. The suspension force is exploited to levitate the rotor avoiding the use of mechanical bearings, and completely eliminating the related friction. Therefore, bearingless machines are particularly convenient in lubricant free applications such as in pharmaceutical, chemical and semiconductor industries [1]–[3] where a perfectly clean environment has to be assured. Full levitating systems could also be employed to achieve high and ultra-high rotational speeds [4], [5], making the BM technology particularly suitable for compressors [6], flywheels [7] and embedded generators [8] where the power density is increased thanks to the high operating speed.

G. Sala is with the Department of Electrical, Electronic and Information Engineering "Guglielmo Marconi", University of Bologna, Bologna (e-mail: giacomo.sala5@unibo.it).

G. Valente, D. Gerada, P. Zanchetta and C. Gerada are with the PEMC group, University of Nottingham, Nottingham.

To the best knowledge of the authors, the first prototype bearingless motor was introduced by Hermann in the middle of 1970s [9], and only in the early 1990s BMs have started being more investigated [10]–[12]. At the early stage of BMs the suspension force and the torque were produced using two separate windings with different pole pairs number [10], [12]. However, because the space needed to host the two separated windings leads to an increase of the machine diameter, more recently designs have been proposed to combine force and torque production in a single winding set [13]–[15]. Among the BM solutions, the multiphase winding typology is one of the most widely adopted [16]–[18].

Multiphase drives are well known for being a suitable solution for high power and safety critical applications such as ship propulsion, locomotive traction, electric vehicles and aircraft [19]–[22]. The enhanced post fault capability of the multiphase layout became a key point also in the research related to bearingless applications. In [23] a six-phase fault tolerant bearingless control of a PM machine is presented. Each phase is supplied by an isolated single-phase converter and the post fault operations are proved with up to two adjacent or opposite open-circuited phases. However, the post fault controllability results infeasible when two inverted or three adjacent phases are open-circuited. A fault tolerant triple three-phase sectored PM machine is described in [24] where the independent $d-$ axis and $q-$axis current control of each winding allows for suspension force and torque generation, respectively. The results presented show that the multiphase BM can operate in case of a three-phase open-circuit fault in one of the three-phase windings.

This paper analyses the same post fault capabilities for a bearingless 18 slot - 6 pole MS-SPM machine with a triple three-phase winding by means of a SV control strategy. MS-SPM machines with a similar multiphase winding structure have been already employed as BMs in [24]–[26], however the suspension force and torque controls are significantly different. In fact, in [24]–[26] the conventional Park transformation of each three-phase machine winding, named sector, is adopted in the control algorithm. On the other hand, the approach proposed in this work in based on the control of those airgap magnetic field space harmonics involved in the radial force and torque generation by means of the current SV technique. The control technique was presented in [17] and applied to a healthy bearingless MS-SPM machine. The extension of the bearingless control to a three-phase open-circuit fault, instead, is the main focus of this work. The presented work deals with the post fault operation of the considered bearingless machine
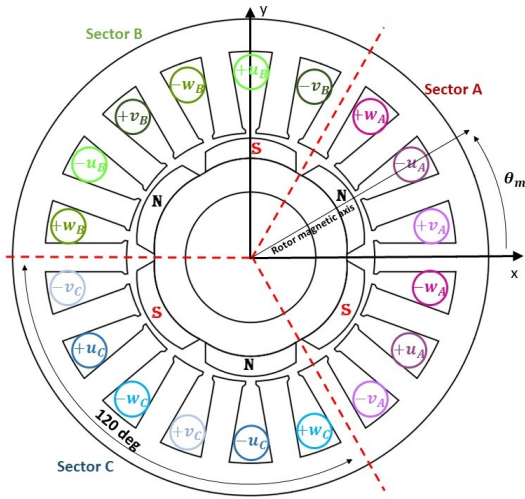
Fig. 1. Cross section of the 18 slot - 6 poles 3 sectors MS-SPM with 3×3 single layer distributed winding.

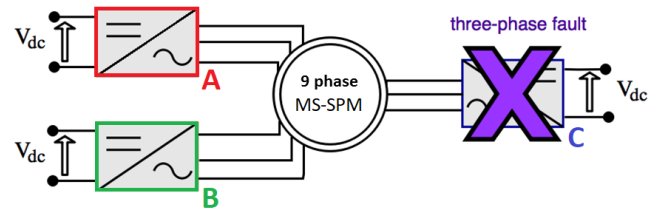| Parameter	Value
Pole number ($2p$)	6
PM material	NdFeB
Power rating	1.5 [kW]
Rated Speed	3000 [rpm]
Rated torque	6 [Nm]
Turns/coil (N_c)	22
Phase resistance (R_{ph})	0.0808 [Ohm]
Line to line voltage constant	15.5 [V/krpm]
PM flux of one sector	0.0284 [Wb]
Torque constant	0.434 [Nm/A]
Outer stator radius	47.5 [mm]
Mid-airgap radius	24.25 [mm]
Axial length	90 [mm]
Airgap length (δ)	1 [mm]
PMs thickness (δ_{PM})	4 [mm]
PM span (Δ_{PM})	2.67 [rad]
angle between two adjacent phases of a sector (α_{ph})	$\pi/9$ [rad]

Fig. 2. Schematic representation of a bearingless triple three-phase MS-SPM machine with one inverter open-circuit fault (inverter C in this figure).

and therefore assumes a proper open-circuit detection strategy capable of promptly switching from healthy to faulty control algorithm. Furthermore, even if a single-phase open-circuit occurs (i.e. one faulty inverter leg or accidental disconnection of one cable) the whole related inverter is disabled. In fact, the single-phase open-circuit fault would result in a more complex model, and the proposed post fault control is a reasonable solution for a multi three-phase drive. On the other hand, aiming to reduce the de-rating of the drive, the investigation of the single-phase open-circuit in a single star layout has been selected as a promising future work as stated in the conclusions.

The machine model and the current SVs needed to generate the required suspension force and torque are presented, at first assuming healthy operating condition. Then, the suspension radial force and motoring torque generation are described and modelled considering the open-circuit fault of a machine three-phase sub-winding. The reference current SVs are calculated from the machine model targeting the minimization of the stator copper losses. Numerical simulations, performed in a Matlab-Simulink environment, have been employed to evaluate the feasibility of the post fault bearingless control, and to compare the control performance with the ones obtained by the algorithm proposed in [27], [28]. Finally, experimental results are displayed to validate the performance of the proposed Post Fault Control (PFC) for a prototype of bearingless MS-SPM machine.

II. THE BEARINGLESS MS-SPM MACHINE

A. The machine structure

The cross section of the prototype bearingless MS-SPM machine considered in this work is shown in Fig. 1. The MS-SPM consists of a conventional permanent magnet machine with a re-arranged winding structure: the original three-phase winding has been replaced with a multiphase one, involving three full-pitched three-phase sub-windings. As can be observed from Fig. 1, each three-phase sub-winding occupies one third of the stator circumference, named sector, without overlapping the others. Finally, the three sub-windings are

independently star connected and are fed by three commercial VSIs, as it is shown in Fig. 2. The main machine design parameters are listed in Table I.

B. The Bearingless Machine operating principles

The $x - y$ axis force components and the torque are the mechanical quantities that have to be independently controlled in order to suspend and rotate the rotor. In [17] an efficient control method has been proposed in order to generate the required suspension force and torque minimizing the copper losses. In healthy conditions the torque can be generated in the same way of a standard three-phase machine, with each sector contributing to one third of the total torque. The radial force, instead, is obtained by the unbalanced control of the three-phase VSIs. The suspension force production principle can be qualitatively explained referring to Fig. 1. The multiphase layout of the system allows to control the airgap flux density in the various sectors to a different set point. This unbalance flux distribution generates the radial force acting on the rotor. As example, in the rotor position of Fig. 1, the $x-$ axis force can be produced by strengthening the airgap flux density in sector A and weakening the ones in the corresponding sectors B and C.

Whereas, if a three-phase open-circuit fault occurs, some currents are forced to be zero. To continue operate the machine, the remaining healthy phases have to be exploited to make still possible the simultaneous control of both the torque and the radial force.

The analytical model of the MS-SPM is derived in the next section, determining the current SVs necessary to control the

suspension force and torque in both healthy and open-circuit conditions. Then, focusing on the drive layout depicted in Fig. 2, a PFC is proposed, aiming for an improvement of the control performance of MS-SPM bearingless machines under one sector open-circuit fault.

III. ANALYTICAL MODEL OF RADIAL FORCE AND TORQUE PRODUCTION

For the sake of clarity, the main subscripts and superscripts employed to define quantities involved in the suspension force and torque modelling are reported below:

A, B, C   Sector/inverter definition (i.e. the sub-winding in sector A is fed by inverter A).

U, V, W   Phase definition in each sector.

2, 3, 4   Spatial harmonic order, in mechanical degrees, of the magnetic field distribution produced by the related current SV.

M, N   Auxiliary current vectors definition (no physical meaning).

A. Healthy condition

In this paragraph, the mechanical quantities (i.e., suspension force and torque) are described in terms of current SVs following the analysis presented in [27]. The model assumes an airgap magnetic field distribution with only radial component, and neglects slotting effect and iron saturation. Under the aforementioned hypotheses, the magnetic field can be evaluated, for each spatial angular position of the airgap ϑ (mechanical degrees), in terms of Fourier series as:

$$H(\vartheta) = \sum_{\rho=1}^{\infty} \Re\{(\bar{H}_{S,\rho} + \bar{H}_{PM,\rho})e^{-j\rho\vartheta}\}, \quad (1)$$

where $\bar{H}_\rho = \bar{H}_{S,\rho} + \bar{H}_{PM,\rho}$ is the ρth component of the Fourier series of the spatial distribution of the magnetic field in the airgap, with the stator contribution:

$$\bar{H}_{S,\rho} = \frac{9N_c sin(\rho\pi/2)}{\pi\delta\rho}\bar{i}_\rho, \quad (2)$$

and the rotor PMs contribution:

$$\bar{H}_{PM,\rho} = \frac{12B_r\delta_{PM}sin(\rho\Delta_{PM}/2)}{\mu_0\pi\delta\rho}e^{j\rho\vartheta_m}, \quad (3)$$

where N_c is the number of turns per phase, δ is the overall magnetic airgap, B_r is the PMs remeneance, δ_{PM} the PM thickness, Δ_{PM} the PM span, ϑ_m the rotor mechanical position, as shown in Fig. 1, and $\bar{i}_\rho$ is the ρth current SV defined, for the analysed machine, as:

$$\bar{i}_\rho = \frac{2}{9}\sum_{Z=A,B,C}(^Z i_U - {}^Z i_V e^{-j\rho\alpha_{ph}} - {}^Z i_W e^{j\rho\alpha_{ph}})e^{j\rho\frac{2\pi}{3}(p_Z-1)}, \quad (4)$$

where α_{ph} is the angle between two adjacent phases of the same sector, Z indicates the sector/inverter ($Z = A, B, C$), and $p_Z = 1, 2, 3$ for $Z = A, B, C$, respectively.

Typically, the main spatial magnetic field harmonic of the PM in the airgap has periodicity equal to the machine pole pair number p. Hence, torque is generated by controlling the current SV related to the same harmonic. On the other hand, the current SVs that produce airgap magnetic fields of periodicity $p-1$ and $p+1$ generate radial force. In the considered machine $p = 3$, hence the spatial harmonic related with the torque production is the 3rd, while the ones related to the force generation are the 2nd and the 4th. It was demonstrated in [27] that the relationship between the mechanical interactions (suspension force and torque) and the current SVs can be given by (5) and (6):

$$\bar{F} = F_x + jF_y = \bar{F}_2 + \bar{F}_4 = k_{F2}\bar{i}_2^* e^{j3\vartheta_m} + k_{F4}\bar{i}_4 e^{-j3\vartheta_m}, \quad (5)$$

and

$$T = k_T i_{3q} = k_T\Im\{\bar{i}_3 e^{-j3\vartheta_m}\}, \quad (6)$$

where i_{3q} is the quadrature axis component of the 3rd current SV in the rotor reference frame, and "*" stands for the complex conjugate. The torque and force constants (k_T, k_{F2}, k_{F4}) can be evaluated analytically following the procedure given in [27] or by FEA.

Finally, the current SVs needed to control the torque and radial force components can be defined as follows:

$$\begin{bmatrix} \bar{i}_2 \\ \bar{i}_4 \\ \bar{i}_3 \end{bmatrix} = \begin{bmatrix} (\bar{F}_2^*/k_{F2})e^{j3\theta_m} \\ (\bar{F}_4/k_{F4})e^{j3\theta_m} \\ j(T_{ref}/k_T)e^{j3\theta_m} \end{bmatrix}, \quad (7)$$

where $\bar{F}_2$ and $\bar{F}_4$ are the two main contributions of the currents control to the radial force, provided by the 2nd and 4th SVs respectively. The optimum control of the two force contributions was already given in [17]. In particular, to control the force with the minimum copper losses, the force contributions have to be controlled as:

$$\begin{aligned} \bar{F}_2 &= F_{2pu}\bar{F}_{ref}, \\ \bar{F}_4 &= (1 - F_{2pu})\bar{F}_{ref}, \end{aligned} \quad (8)$$

with F_{2pu} the optimal ratio between the 2nd and 4th SVs in the force production ($F_{2pu} = 0.236$ for the analysed machine). In order to describe the suspension force and torque generation as a function of the nine phase currents, it is convenient to relate the current SVs, introduced in (5) and (6), with the three-phase ones. The latter ones can be obtained for a generic sector Z applying the direct Clarke transformation defined as:

$$^Z\bar{i} = \frac{2}{3}(^Z i_U + {}^Z i_V e^{j\frac{2\pi}{3}} + {}^Z i_W e^{-j\frac{2\pi}{3}}). \quad (9)$$

The phase currents of each sector can be obtained applying the inverse Clarke transformation to (9). Then, the phase currents expressions can be replaced in (4) in order to relate the 3rd current SV to the three-phase ones as follows:

$$\bar{i}_3 = \frac{1}{3}(^A\bar{i} + {}^B\bar{i} + {}^C\bar{i}), \quad (10)$$

whereas the relationship between the 2nd and 4th current SVs with the three-phase ones is found as:

$$\begin{aligned} \bar{i}_2 &= \frac{1}{3}(\bar{i}_N c_{m2} + \bar{i}_M^* c_{n2}), \\ \bar{i}_4 &= \frac{1}{3}(\bar{i}_M c_{m2} + \bar{i}_N^* c_{n4}), \end{aligned} \quad (11)$$

where $\bar{i}_M$ and $\bar{i}_N$ are auxiliary current vectors defined in (12).

$$\begin{aligned}
\bar{i}_M &= \frac{1}{3}\left({}^A\bar{i} + {}^B\bar{i}e^{j\frac{2\pi}{3}} + {}^C\bar{i}e^{-j\frac{2\pi}{3}}\right), \\
\bar{i}_N &= \frac{1}{3}\left({}^A\bar{i} + {}^B\bar{i}e^{-j\frac{2\pi}{3}} + {}^C\bar{i}e^{j\frac{2\pi}{3}}\right).
\end{aligned} \tag{12}$$

The constants c_{m2}, c_{n2} and c_{n4} are defined in Appendix.

B. Faulty condition

The open-circuit fault of one machine sector can be taken into account by zeroing the related three-phase current vector defined by (9).

The three-phase current vector ${}^Z\bar{i}$ in (9) can be written, in terms of $\bar{i}_3$ and the auxiliary current vectors $\bar{i}_M$ and $\bar{i}_M$, manipulating (10) and (12) as follows:

$$^Z\bar{i} = \bar{i}_3 + \bar{i}_M e^{-j\frac{2\pi}{3}(pz-1)} + \bar{i}_N e^{j\frac{2\pi}{3}(pz-1)}. \tag{13}$$

Therefore, a fault in the generic machine sector Z can be modelled in terms of current SVs by imposing (13) equal to zero:

$$\bar{i}_3 + \bar{i}_M e^{-j\frac{2\pi}{3}(pz-1)} + \bar{i}_N e^{j\frac{2\pi}{3}(pz-1)} = 0. \tag{14}$$

The aforementioned constraint makes $\bar{i}_3$, $\bar{i}_M$ and $\bar{i}_N$, and consequently the force and the torque, no more independently controllable.

It is now convenient, for the analysis of the open fault, to rewrite the suspension force equation (5) explicating the auxiliary variables $\bar{i}_M$ and $\bar{i}_N$ as in (15).

$$\begin{aligned}
\bar{F} =& \frac{1}{3}[k_{F2}c_{n2}e^{j3\vartheta_m} + k_{F4}c_{m2}e^{-j3\vartheta_m}]\bar{i}_M + \\
& + \frac{1}{3}[k_{F2}c_{m2}e^{j3\vartheta_m} + k_{F4}c_{n4}e^{-j3\vartheta_m}]\bar{i}_N^*.
\end{aligned} \tag{15}$$

Equations (6) and (15) together with the constraint (14) are employed to develop the post fault algorithm presented in the next section.

IV. FAULT TOLERANT CONTROL

A. Previous Fault Tolerant Control

In [28] a PFC of the drive was proposed. The method was based on the assumption that the $d-$axis component of the 3rd current SV was set equal to zero in the PFC. Hence, the expression of $\bar{i}_3$ as a function of the reference torque T_{ref} was calculated as:

$$\bar{i}_3 = (i_{3d} + ji_{3q})e^{j3\vartheta_m} = \left(j\frac{T_{ref}}{k_T}\right)e^{j3\vartheta_m}. \tag{16}$$

Replacing (16) in (14) yields:

$$j\frac{T_{ref}}{k_T}e^{j3\vartheta_m} + \bar{i}_M e^{-j\frac{2\pi}{3}(pz-1)} + \bar{i}_N e^{j\frac{2\pi}{3}(pz-1)} = 0. \tag{17}$$

The system of equations (17) and (15) can be solved for $\bar{i}_M$ and $\bar{i}_N$. The latter ones are replaced in (11) obtaining the expressions of $\bar{i}_2$ and $\bar{i}_4$ as a function of the reference force $\bar{F}_{ref}$ and torque T_{ref}.

B. New Optimised Fault Tolerant Control

In the proposed PFC, the $d-$axis component of the 3rd current SV is obtained considering the machine copper losses minimization. The stator copper losses can be computed as the sum of the losses of the three three-phase subsystems as:

$$P_{cu} = \sum_{Z=A,B,C} \frac{3}{2}R_{ph}\,{}^Z\bar{i}\,{}^Z\bar{i}^* = \frac{3}{2}R_S\left({}^A\bar{i}\,{}^A\bar{i}^* + {}^B\bar{i}\,{}^B\bar{i}^* + {}^C\bar{i}\,{}^C\bar{i}^*\right), \tag{18}$$

where R_{ph} is the phase resistance.
Replacing (13) in (18) and manipulating the equation it is possible to write the expression of the copper losses as a function of $\bar{i}_3$, $\bar{i}_M$ and $\bar{i}_N$ as follows:

$$\begin{aligned}
P_{cu} = \sum_{Z=A,B,C} \frac{3}{2}R_S([\bar{i}_3 + \bar{i}_M e^{-j\frac{2\pi}{3}(pz-1)} + \bar{i}_N e^{j\frac{2\pi}{3}(pz-1)}] \\
[\bar{i}_3 + \bar{i}_M e^{-j\frac{2\pi}{3}(pz-1)} + \bar{i}_N e^{j\frac{2\pi}{3}(pz-1)}]^*).
\end{aligned} \tag{19}$$

The optimum i_{3d} value can be computed by solving the equation

$$\frac{dP_{cu}}{di_{3d}} = 0, \tag{20}$$

after writing the expression of P_{cu} as a function of i_{3d}, T_{ref} and $\bar{F}_{ref}$ only. In particular, $\bar{i}_3$ can be replaced by:

$$\bar{i}_3 = \left(i_{3d} + j\frac{T_{ref}}{k_T}\right)e^{j3\vartheta_m}, \tag{21}$$

while $\bar{i}_M$ and $\bar{i}_N$ can be computed solving the system containing equations (14) and (15) substituting $\bar{i}_3$ with (21) and $\bar{F}$ with its reference value $\bar{F}_{ref}$. The expression of i_{3d} that minimizes the copper losses for an open-circuit fault in sector A is reported in (22).

$$i_{3d} = \frac{\Re\{(\bar{B}_1\bar{B}_2^* + \bar{C}_1\bar{C}_2^*)\bar{i}_{FC}\}}{\bar{B}_2\bar{B}_2^* + \bar{C}_2\bar{C}_2^*}, \tag{22}$$

with:

$$\bar{i}_{FC} = \frac{3\bar{F}_{ref} + \bar{K}_{F^*}\bar{F}_{ref}^* + (j\bar{K}_3 e^{j3\vartheta_m} - j\bar{K}_{3^*}e^{-j3\vartheta_m})\frac{T_{ref}}{k_T}}{\bar{K}_D}, \tag{23}$$

where $\bar{K}_{F^*}$, $\bar{K}_3$, $\bar{K}_{3^*}$, $\bar{K}_D$, $\bar{B}_1$, $\bar{B}_2$, $\bar{C}_1$ and $\bar{C}_2$ are defined in the Appendix. A similar procedure can be followed to compute i_{3d} in case of a fault in sector B or C.
The expressions of $\bar{i}_M$ and $\bar{i}_N$ can be obtained solving again the system of equations (14) and (15) where i_{3d} is now completely defined by (22). The expression of $\bar{i}_M$ is reported in:

$$\bar{i}_M = \bar{i}_{FC} + \frac{\bar{K}_3 e^{j3\vartheta_m} + \bar{K}_{3^*}e^{-j3\vartheta_m}}{\bar{K}_D}i_{3d}, \tag{24}$$

while $\bar{i}_N$ can be obtained from (15).
Finally, the reference SVs $\bar{i}_2$ and $\bar{i}_4$ are determined by (11) to implement the current control needed for the desired torque and suspension force. Equations (22) - (24) define the optimal reference currents in the PFC algorithm once the reference torque and force components are known. In the next section it is shown, by numerical simulations, that, without a control improvement based on the copper losses minimisation the increase of phase currents, and consequently copper losses,

significantly deteriorates the post fault bearingless operation of the drive.

V. NUMERICAL SIMULATION RESULTS

A. Description of the simulation model

The control of the bearingless drive has been implemented in Matlab-Simulink, in order to simulate the bearingless performance in healthy and faulty operating conditions.
The simulated machine model is FE based, derived by means of multi-static non-linear FE simulations in MagNet. The FE model of the machine in Fig. 1 is based on the parameters listed in Table I. For each static simulation the rotor is rotated by a small angle ($\Delta\vartheta$) and each sector is fed with current values ranging from $-i_{rated} \div i_{rated}$ (with 1 A steps). The obtained $x-y$ force components and torque are stored in the form of lookup table in the Simulink model and a linear method has been used to interpolate the lookup table elements. This model has the advantage of allowing simulating the control algorithm without the need of FE co-simulations with a good accuracy as the non-linearities of the materials are considered. Fig. 3 shows a view of the FE analysis carried out for the development and validation of the machine model employed in the Matlab-Simulink simulation in both healthy and faulty conditions.
The scheme of the closed-loop bearingless control for the analysed drive is presented in Fig. 4. Two outer control loops can be identified in the scheme: for the speed and the radial position control respectively. It can be noticed that the reference $x-y$ axis positions are set equal to zero, for the suspension of the rotor in the centre of the stator. The speed reference, instead, can be set by the user. The outputs of the speed and radial position controllers are the torque and $x-y$ force components respectively. These reference torque and force are the inputs of the current SVs calculation block, where reference current SVs are evaluated according to the equations described in Sections III-A and IV-B, for the healthy and faulty drive respectively. Then, as in a field oriented control of a three-phase drive, the six $d-q$ axis current SV components are the input for the respective PI regulators. The current regulator outputs are the $d-q$ axis voltage SVs, transformed by means of the inverse SV transformation into the three three-phase reference voltages (conveniently modulated for supplying the nine-phase machine terminals).
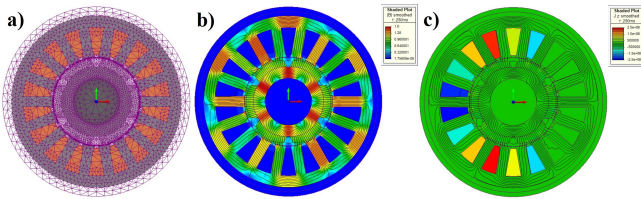

Fig. 3. Finite Element geometry of the analysed machine: FE mesh (a), view of the flux density distribution (b) and instantaneous phase current densities (c). The views are related to the simulated post fault operation.
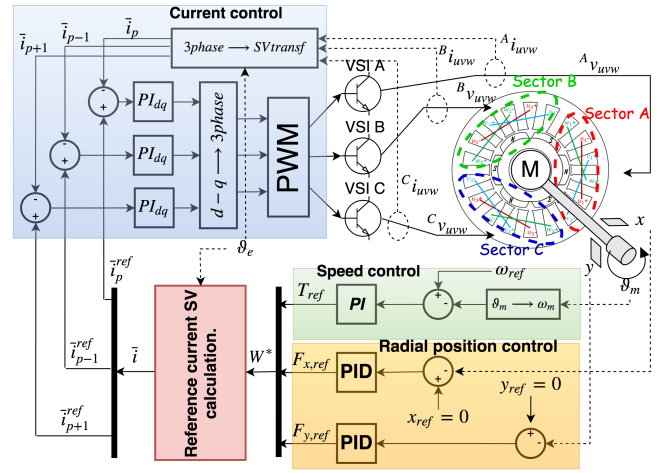

Fig. 4. Overall closed-loop control scheme of the bearingless MS-SPM.

B. Simulation Results

Fig. 6 and 5 present the simulation results. In particular, the PFC algorithm explained in IV-B is compared with the healthy operation and with the PFC algorithm proposed in [28], where the minimization of the copper losses was not considered. The simulated operating conditions (torque, speed and radial force acting on the rotor) can be deduced from Fig. 5-(a,b,c). The PFCs are compared for 6 Nm torque and 200 N constant weight force on the shaft. The machine is speed controlled at 3000 rpm and the radial position control is active during all the simulation time. The 6 Nm load is applied after the machine reaches the rated speed. The machine is healthy until 0.1 s, then inverter A is disabled causing an open-circuit fault. At 0.1 s the control algorithm changes its reference currents to take into account for the faulty condition: from 0.1 to 0.2 s the control is the non-optimised PFC ($i_{d3} = 0$); from 0.2 until 0.3 s the control is the proposed optimised PFC (with the value of i_{d3} controlled in order to minimise the copper losses, i.e., obtained by (22)). Fig. 5-(h,i,l) show the 2nd, 3rd and 4th current SVs respectively. In particular, it can be observed from Fig. 5-i that i_{d3} is equal to zero in the non-optimised PFC, while it is controlled to its optimal value in the proposed one. The advantage of the new control in terms of copper loss reduction is highlighted in Fig. 5-d.
From the simulation results it can be noticed that the bearingless operation can be theoretically achieved during an open-circuit fault with both the PFCs, but as expected the optimised one allows for significantly reducing the phase currents (see Fig. 5-(e, f, g)) and consequently the stator copper losses. Furthermore, the radial force ripple is lower as it can be observed in Fig. 5-c. Fig. 6 compares the steady state $x-y$ position trajectories obtained with the two PFC algorithms with the trajectory in healthy operation. Even if the position displacement is really small in the simulation, it is already possible to notice a better control performance with the proposed control (named as "new optimised PFC" in Fig. 6). The difference on the performance between the two controls is caused by an undesired effect, named as radial force ripple. This force ripple is caused by the interactions of the higher order field harmonics.
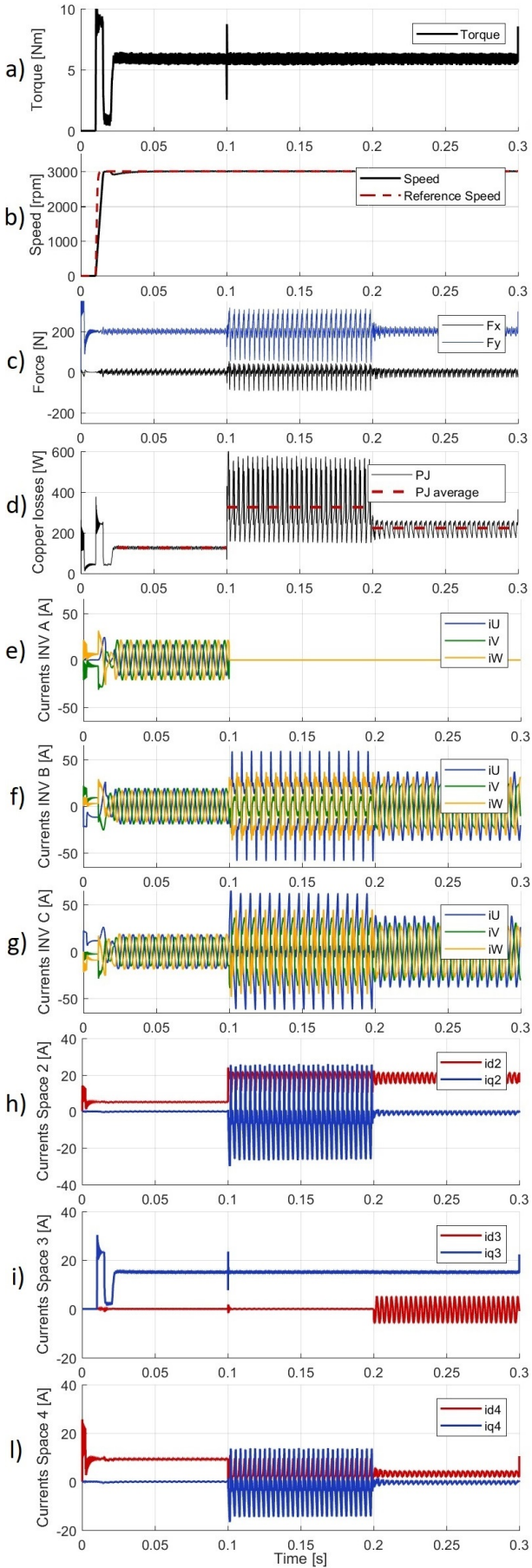
Fig. 5. Simulation results: a) reference torque; b) rotating speed; c) $x-y$ axis reference force components; d) stator copper losses; e) phase currents of sector A; f) phase currents of sector B; g) phase currents of sector C; h) 2nd current SV; i) 3rd current SV; l) 4th current SV.
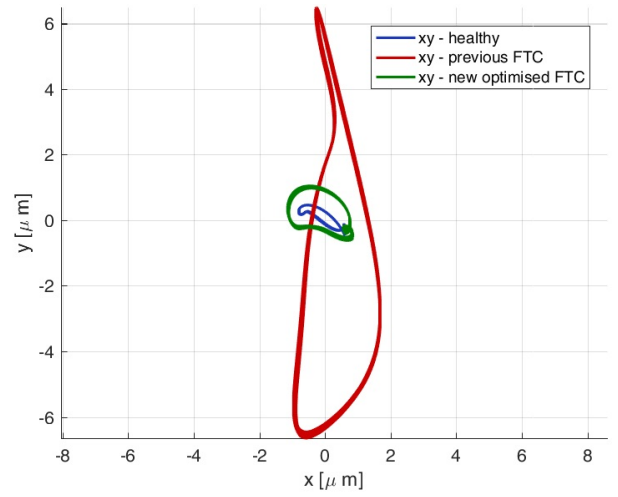

Fig. 6. Simulation result of the $x-y$ axis trajectory of the rotor in healthy and faulty operating conditions.

In [27] these interactions have been investigated, showing that when higher currents are applied to control the radial force its ripple becomes more significant. A similar effect appears if the PM machine is controlled in torque ($\bar{i}_2 = \bar{i}_4 = 0$ and $i_{3q} = (T_{ref}/k_T)$) with a significant d-axis current (i_{3d}). The increase of the current, caused by the d-axis component, does not generate torque interacting with the main field harmonic of the magnets $\bar{H}_{PM,3}$, but it produces torque ripple interacting with the asynchronous higher order field harmonics (such as $\bar{H}_{PM,15}$, $\bar{H}_{PM,21}$, $\bar{H}_{PM,33}$, etc.).

VI. EXPERIMENTAL TESTS

A. Description of the experimental rig

Fig. 7 reveals the experimental rig used to validate the PFC algorithm proposed in this manuscript. Fig. 7-a shows the bearingless MS-SPM machine coupled through a universal joint to a DC load in order to perform the experimental tests. In Fig. 7-b the multiphase sectored winding structure is highlighted. The three three-phase inverters are displayed in Fig 7-c. The power module of the single inverter is a "dual-in-line package intelligent power module (PS21A79)" manufactured by Mitsubishi Semiconductor. The switching frequency and dead times of the IGBTs are set equal to 10 kHz and 2.2 μs, respectively. A custom made control platform (uCube) [29] shown in Fig. 7-d communicates with the power module gate drives, by means of fibre optic cables. Two DoF are actively controlled in the proposed bearingless MS-SPM machine. Therefore, the tilting and axial movements are constrained by means of a self-alignment bearing installed on one side of the shaft. The other side is free to move along the $x-y$ axis within the displacement given by the backup bearing clearance (150 μm). Two $x-y$ axis displacement sensors are installed on the backup bearing side of the shaft (as shown in Fig. 7-e), and employed to measure the position feedbacks for the radial position PID regulators.

B. Experimental results

Experimental tests were performed for a two DoF bearingless operation of the machine. In particular, Fig. 9 and 8 show the behaviour of the machine controlled in torque at about half the rated torque (2.5 Nm reference value). The shaft if connected to the DC drive rotating at the rated speed. The machine starts operating in healthy condition, and at 33 ms time the IGBTs of inverter A are disabled in order to cause a three-phase open-circuit fault. At the same time of the fault, the control algorithm switches from healthy to faulty. The fault lasts for 33 ms and at 66 ms the IGBTs are enabled again, restoring the healthy operating conditions of the drive. This test is performed in order to validate the capability of the drive to continuously operate if a fault occurs and when the latter is extinguished (i.e., the faulty inverter can be replaced or reactivated).

Fig. 9-(a, b, c) present the machine operating conditions in terms of reference torque, speed and $x - y$ radial force components. Fig. 9-d shows the copper losses produced by the phase currents in Fig. 9-(e, f, g). It can be noticed that the copper losses double from 14.5 W to 28.5 W during the fault. Therefore, as expected, a de-rating of the output power is mandatory to continuously operate in faulty conditions.

Looking at the current SVs in Fig. 9-(h, i, l), the i_{d3} component changes its value from 0 to the optimised value required by the optimised PFC algorithm when the fault appears. It is worth noticing that only the experimental results obtained with the optimised PFC algorithm are presented. In fact, the current references generated by the non-optimised PFC are significantly higher and not sustainable with the employed inverter power modules. The reason of such an important increase of losses with the non optimised method is due to the fact that in case of fault there are four degrees of freedom in the current control. Therefore, to generate the reference force and torque there is only one remaining degree of freedom in the current control, and its exploitation with or without the minimisation of the copper losses makes a significant difference.

Fig. 10 shows the simulation results obtained with the same operating conditions of the experimental test shown in Fig. 9. It can be noticed that the $x - y$ force components obtained in the experimental test (Fig. 9 -c) have a higher ripple if compared to simulation results (Fig. 10 -c). The reason for this is the simplified mechanical system adopted in the simulation model [30] if compared to the real one where mass unbalances in the rotor cause the $x - y$ axis PID position controllers, designed in [30], to react producing non-constant $x - y$ force components. The force ripple, together with the inverter non-linearities and high frequency noise coming from the $x - y$ axis displacement probes, is then responsible for the distortion of the currents (Fig. 9 -e to -l)).

Finally, the $x - y$ position trajectories for both healthy and faulty operating conditions are presented in Fig. 8 showing a maximum displacement of 11 μm, hence experimentally validating the proposed PFC method. Indeed, the good match in the two trajectories reflects the effectiveness of the open-circuit PFC method proposed. The difference between healthy and faulty operations can be appreciated observing the phase currents in Fig. 9 -e to -g. Indeed, when an open-circuit fault occurs in sector A the related phase currents go to zero (see Fig. 9 - e between 33 and 66 ms) while the phase currents increase in the remaining healthy sectors (see Fig. 9 -f and -g during the same time) in order to compensate the loss of one sector to the suspension force and torque contribution.
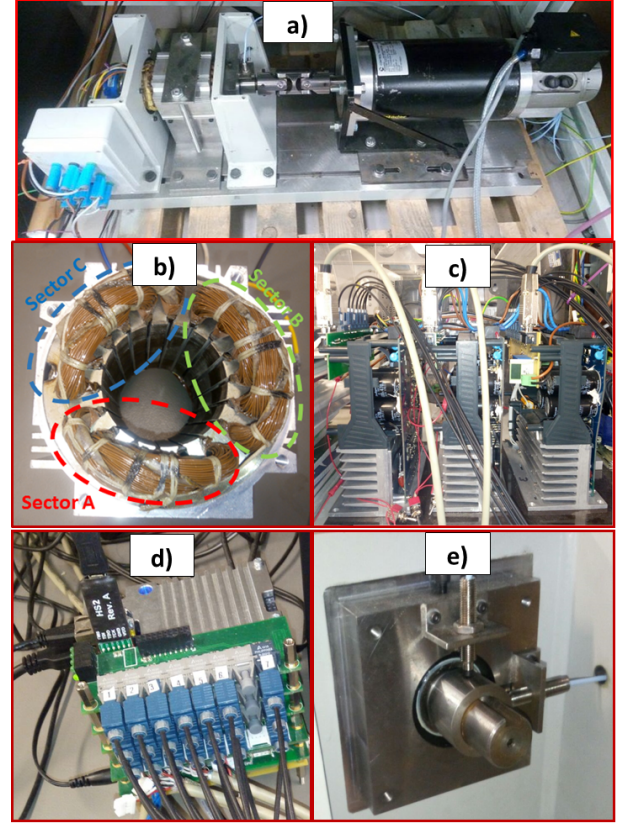

Fig. 7. Experimental rig in all its parts: a) prototype MS-SPM machine (left hand side) coupled with the DC load (right hand side); b) stator of the MS-SPM machine and multiphase winding structure; c) three three-phase inverters; d) uCube control board e) $x - y$ axis displacement sensors mounted on the probe supports.
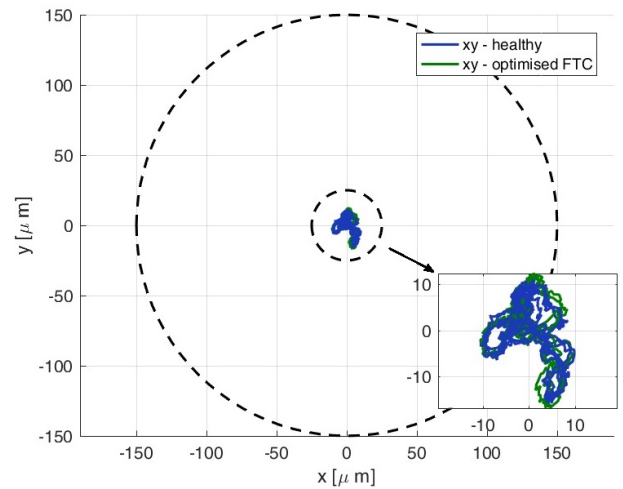

Fig. 8. Experimental result of the $x - y$ axis trajectory of the rotor in healthy and faulty operating conditions.
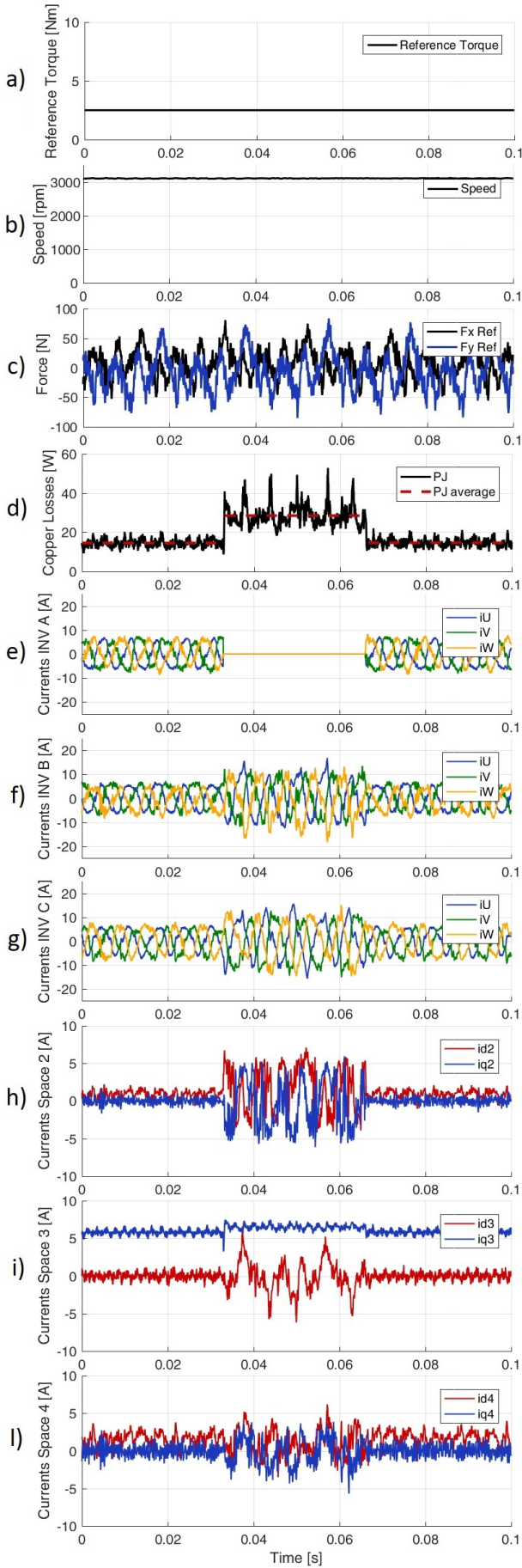
Fig. 9. Experimental results: a) reference torque; b) rotating speed; c) $x - y$ axis reference force components; d) stator copper losses; e) phase currents of sector A; f) phase currents of sector B; g) phase currents of sector C; h) 2nd current SV; i) 3rd current SV; l) 4th current SV.
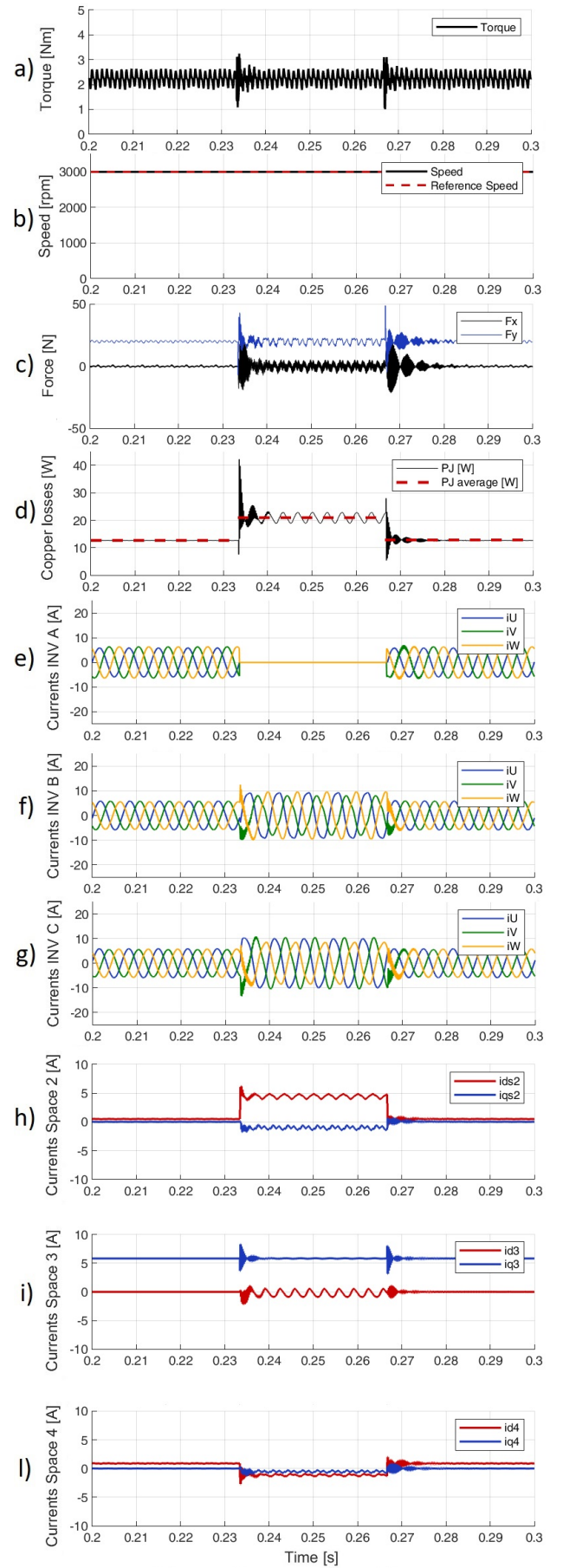
Fig. 10. Simulated results: a) torque; b) rotating speed; c) $x - y$ axis force components; d) stator copper losses; e) phase currents of sector A; f) phase currents of sector B; g) phase currents of sector C; h) 2nd current SV; i) 3rd current SV; l) 4th current SV.

VII. Conclusion

This work presents an optimised PFC algorithm for a bearingless triple three-phase permanent magnet machine under one inverter open-circuit fault. The equations describing the electrical machine and its control, in healthy and faulty operations, are provided. The control was simulated and compared with a previously published PFC.

The simulated results highlight the advantages of the proposed solution, highlighting the importance of the optimisation algorithm by exploiting all the available DoF in the current control. However, it is clear that a de-rating of the output power is still required when a fault occurs, because the efficiency of the radial force control in case of fault is lower and because the required torque has to be produced by the remaining healthy phases.

Experimental tests were carried out on a drive prototype to validate the controllability of the faulty drive. The results show that the proposed PFC allows for a stable and performing bearingless operation of the machine, and for a fast recovery of the system when the open phases are reconnected/reactivated. The tests validated the simulation results and the feasibility of the proposed PFC algorithm.

Future works that have been identified as promising would consist of extending the presented three-phase open-circuit model in order to consider single-phase open-circuit and three-phase short circuit faults.

Appendix

The constants in (11) are defined as:

$$
\begin{aligned}
c_{m2} &= 1 - e^{-j\left(\frac{2\pi}{3} + \frac{2\pi}{9}\right)} - e^{j\left(\frac{2\pi}{3} + \frac{2\pi}{9}\right)}, \\
c_{n2} &= 1 - e^{j\left(\frac{2\pi}{3} - \frac{2\pi}{9}\right)} - e^{-j\left(\frac{2\pi}{3} - \frac{2\pi}{9}\right)}, \\
c_{n4} &= 1 - e^{j\left(\frac{2\pi}{3} - 4/9\pi\right)} - e^{-j\left(\frac{2\pi}{3} - 4/9\pi\right)}.
\end{aligned}
\tag{25}
$$

The variables in (23) depend on the rotor position and the faulty sector, and are calculated as:

$$
\begin{aligned}
K_{F*} &= 3\frac{k_{F2}c_{m2}e^{j3\vartheta_m} + k_{F4}c_{n4}e^{-j3\vartheta_m}}{k_{F2}c_{n2}e^{-j3\vartheta_m} + k_{F4}c_{m2}e^{j3\vartheta_m}}e^{-j\frac{2\pi}{3}(p_Z-1)}, \\
\bar{K}_3 &= \frac{|(k_{F2}c_{m2}e^{j3\vartheta_m} + k_{F4}c_{n4}e^{-j3\vartheta_m})|^2}{k_{F2}c_{n2}e^{-j3\vartheta_m} + k_{F4}c_{m2}e^{j3\vartheta_m}}e^{j\frac{2\pi}{3}(p_Z-1)}, \\
\bar{K}_{3*} &= (k_{F2}c_{m2}e^{j3\vartheta_m} + k_{F4}c_{n4}e^{-j3\vartheta_m})e^{j\frac{2\pi}{3}(p_{zf}-1)}, \\
\bar{K}_D &= (k_{F2}c_{n2}e^{j3\vartheta_m} + k_{F4}c_{m2}e^{-j3\vartheta_m}) + \\
&\quad - \frac{|(k_{F2}c_{m2}e^{j3\vartheta_m} + k_{F4}c_{n4}e^{-j3\vartheta_m})|^2}{k_{F2}c_{n2}e^{-j3\vartheta_m} + k_{F4}c_{m2}e^{j3\vartheta_m}}.
\end{aligned}
\tag{26}
$$

Finally, the variables in (22) are evaluated as:

$$
\begin{aligned}
\bar{B}_1 &= e^{-j\frac{2\pi}{3}} - e^{j\frac{2\pi}{3}}, \\
\bar{B}_2 &= \frac{\bar{K}_{3*}e^{-j3\vartheta_m} + \bar{K}_3 e^{j3\vartheta_m}}{\bar{K}_D}\bar{B}_1 + (1 - e^{j\frac{2\pi}{3}})e^{j3\vartheta_m}, \\
\bar{C}_1 &= e^{j\frac{2\pi}{3}} - e^{-j\frac{2\pi}{3}}, \\
\bar{C}_2 &= \frac{\bar{K}_{3*}e^{-j3\vartheta_m} + \bar{K}_3 e^{j3\vartheta_m}}{\bar{K}_D}\bar{C}_1 + (1 - e^{j\frac{2\pi}{3}})e^{j3\vartheta_m}.
\end{aligned}
\tag{27}
$$

References

[1] Y. Okada, N. Yamashiro, K. Ohmori, T. Masuzawa, T. Yamane, Y. Konishi, and S. Ueno, "Mixed flow artificial heart pump with axial self-bearing motor," *IEEE/ASME Transactions on Mechatronics*, vol. 10, no. 6, pp. 658–665, Dec 2005.

[2] T. Reichert, T. Nussbaumer, and J. W. Kolar, "Bearingless 300-w pmsm for bioreactor mixing," *IEEE Transactions on Industrial Electronics*, vol. 59, no. 3, pp. 1376–1388, March 2012.

[3] B. Warberger, R. Kaelin, T. Nussbaumer, and J. W. Kolar, "50-nm/2500-w bearingless motor for high-purity pharmaceutical mixing," *IEEE Transactions on Industrial Electronics*, vol. 59, no. 5, pp. 2236–2247, May 2012.

[4] T. Baumgartner, R. M. Burkart, and J. W. Kolar, "Analysis and design of a 300-w 500000-r/min slotless self-bearing permanent-magnet motor," *IEEE Transactions on Industrial Electronics*, vol. 61, no. 8, pp. 4326–4336, Aug 2014.

[5] H. Mitterhofer, W. Gruber, and W. Amrhein, "On the high speed capacity of bearingless drives," *IEEE Transactions on Industrial Electronics*, vol. 61, no. 6, pp. 3119–3126, June 2014.

[6] R. P. Jastrzebski, P. Jaatinen, O. Pyrhnen, and A. Chiba, "Design of 6-slot inset pm bearingless motor for high-speed and higher than 100kw applications," in *2017 IEEE International Electric Machines and Drives Conference (IEMDC)*, May 2017, pp. 1–6.

[7] M. Ooshima, S. Kobayashi, and H. Tanaka, "Magnetic suspension performance of a bearingless motor/generator for flywheel energy storage systems," in *IEEE PES General Meeting*, July 2010, pp. 1–4.

[8] A. Chiba, T. Fukao, O. Ichikawa, M. Oshima, M. Takemoto, and D. G. Dorrell, *Magnetic bearings and bearingless drives*. Elsevier, 2005.

[9] P. Hermann, "A radial active magnetic bearing," *London Patent*, no. 1, p. 478, 1973.

[10] A. Chiba, M. A. Rahman, and T. Fukao, "Radial force in a bearingless reluctance motor," *IEEE Transactions on Magnetics*, vol. 27, no. 2, pp. 786–790, March 1991.

[11] J. Bichsel, "The bearingless electrical machine," 1992.

[12] A. Chiba, T. Deido, T. Fukao, and M. A. Rahman, "An analysis of bearingless ac motors," *IEEE Transactions on Energy Conversion*, vol. 9, no. 1, pp. 61–68, Mar 1994.

[13] W. K. S. Khoo, K. Kalita, and S. D. Garvey, "Practical implementation of the bridge configured winding for producing controllable transverse forces in electrical machines," *IEEE Transactions on Magnetics*, vol. 47, no. 6, pp. 1712–1718, June 2011.

[14] R. Oishi, S. Horima, H. Sugimoto, and A. Chiba, "A novel parallel motor winding structure for bearingless motors," *IEEE Transactions on Magnetics*, vol. 49, no. 5, pp. 2287–2290, May 2013.

[15] E. L. Severson, R. Nilssen, T. Undeland, and N. Mohan, "Design of dual purpose no-voltage combined windings for bearingless motors," *IEEE Transactions on Industry Applications*, vol. 53, no. 5, pp. 4368–4379, Sept 2017.

[16] J. Huang, B. Li, H. Jiang, and M. Kang, "Analysis and control of multiphase permanent-magnet bearingless motor with a single set of half-coiled winding," *IEEE Transactions on Industrial Electronics*, vol. 61, no. 7, pp. 3137–3145, July 2014.

[17] G. Sala, G. Valente, A. Formentini, L. Papini, D. Gerada, P. Zanchetta, A. Tani, and C. Gerada, "Space vectors and pseudoinverse matrix methods for the radial force control in bearingless multisector permanent magnet machines," *IEEE Transactions on Industrial Electronics*, vol. 65, no. 9, pp. 6912–6922, Sept 2018.

[18] B. Li, J. Huang, H. Liu, and Z. Hou, "Analysis and control of seven-phase permanent-magnet bearingless motor with single set of half-coiled winding," in *2014 IEEE 23rd International Symposium on Industrial Electronics (ISIE)*, June 2014, pp. 2080–2086.

[19] E. Levi, R. Bojoi, F. Profumo, H. A. Toliyat, and S. Williamson, "Multiphase induction motor drives - a technology status review," *IET Electric Power Applications*, vol. 1, no. 4, pp. 489–516, July 2007.

[20] A. Cavagnino, A. Tenconi, and S. Vaschetto, "Experimental characterization of a belt-driven multiphase induction machine for 48-v automotive applications: Losses and temperatures assessments," *IEEE Transactions on Industry Applications*, vol. 52, no. 2, pp. 1321–1330, March 2016.

[21] J. Dai, S. W. Nam, M. Pande, and G. Esmaeili, "Medium-voltage current-source converter drives for marine propulsion system using a dual-winding synchronous machine," *IEEE Transactions on Industry Applications*, vol. 50, no. 6, pp. 3971–3976, Nov 2014.

[22] C. Bassi, A. Tessarolo, R. Menis, and G. Sulligoi, "Analysis of different system design solutions for a high-power ship propulsion synchronous motor drive with multiple pwm converters," in *Electrical Systems for Aircraft, Railway and Ship Propulsion*, Oct 2010, pp. 1–6.

[23] X. L. Wang, Q. C. Zhong, Z. Q. Deng, and S. Z. Yue, "Current-controlled multiphase slice permanent magnetic bearingless motors with open-circuited phases: Fault-tolerant controllability and its verification," *IEEE Transactions on Industrial Electronics*, vol. 59, no. 5, pp. 2059–2072, May 2012.

[24] M. Ooshima, A. Kobayashi, and T. Narita, "Stabilized suspension control strategy at failure of a motor section in a d-q axis current control bearingless motor," in *2015 IEEE Industry Applications Society Annual Meeting*, Oct 2015, pp. 1–7.

[25] G. Valente, L. Papini, A. Formentini, C. Gerada, and P. Zanchetta, "Radial force control of multisector permanent-magnet machines for vibration suppression," *IEEE Transactions on Industrial Electronics*, vol. 65, no. 7, pp. 5395–5405, July 2018.

[26] G. Valente, A. Formentini, L. Papini, C. Gerada, and P. Zanchetta, "Performance improvement of bearingless multisector pmsm with optimal robust position control," *IEEE Transactions on Power Electronics*, vol. 34, no. 4, pp. 3575–3585, April 2019.

[27] G. Sala, D. Gerada, C. Gerada, and A. Tani, "Radial force control for triple three-phase sectored spm machines. part i: Machine model," in *2017 IEEE Workshop on Electrical Machines Design, Control and Diagnosis (WEMDCD)*, April 2017, pp. 193–198.

[28] ——, "Radial force control for triple three-phase sectored spm machines. part ii: Open winding fault tolerant control," in *2017 IEEE Workshop on Electrical Machines Design, Control and Diagnosis (WEMDCD)*, April 2017, pp. 275–280.

[29] A. Galassini, G. L. Calzo, A. Formentini, C. Gerada, P. Zanchetta, and A. Costabeber, "ucube: Control platform for power electronics," in *2017 IEEE Workshop on Electrical Machines Design, Control and Diagnosis (WEMDCD)*, April 2017, pp. 216–221.

[30] G. Valente, A. Formentini, L. Papini, P. Zanchetta, and C. Gerada, "Position control study of a bearingless multi-sector permanent magnet machine," in *IECON 2017 - 43rd Annual Conference of the IEEE Industrial Electronics Society*, Oct 2017, pp. 8808–8813.

D. Gerada received the Ph.D. degree in high-speed electrical machines from the University of Nottingham, Nottingham, UK in 2012. From 2007-2016 he was with the R&D Department at Cummins, first as an Electromagnetic Design Engineer (2007-2012), and then as a Senior Electromagnetic Design Engineer and Innovation Leader (2012-2016). At Cummins he pioneered the design and development of high speed electrical machines, transforming a challenging technology into a reliable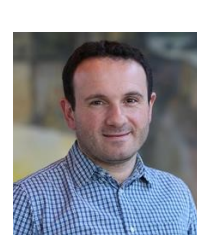 one suitable for the transportation market, while establishing industry-wide used metrics for such machinery. In 2016 he joined the University of Nottingham as a Senior Fellow in Electrical Machines, responsible for developing state of the art electrical machines for future transportation which push existing technology boundaries, while propelling the new technologies to higher technology readiness levels (TRL). Dr. Gerada is a Chartered Engineer in the U.K. and a member of the Institution of Engineering and Technology.

P. Zanchetta (M 00, SM 15) received his MEng degree in Electronic Engineering and his Ph.D. in Electrical Engineering from the Technical University of Bari (Italy) in 1993 and 1997 respectively. In 1998 he became Assistant Professor of Power Electronics at the same University. In 2001 he became lecturer in control of power electronics systems in the PEMC research group at the University of Nottingham UK, where he is now Professor in Control of Power Electronics systems. He has published over 270 peer reviewed papers and he is Senior Member of the IEEE. He is Chair of the IAS Industrial Power Converter Committee IPCC and member of the European Power Electronics (EPE) executive board. His research interests include control of power converters and drives, Matrix and multilevel converters, power electronics for energy and transportation.

G. Sala was born in Vercelli, Italy, in 1990. He received the B. Sc. in Power Engineering in 2012, the M. Sc. degree with honors in Electrical Engineering in 2014, and the Ph. D. in Electrical Machines and Drives in 2018 from the University of Bologna, Bologna, Italy. He was a researcher with the Department of Electrical and Electronic Engineering (PEMC group), at The University of Nottingham, until 2019. He joined the Department of Electric, Electronic and Information Engineering G. Marconi, University of Bologna, where he has been a research fellow since 2019. His research interests include design, modelling and control of multiphase machines for high power systems with high performance and reliability requirements.

C. Gerada (M 05) received the Ph.D. degree in numerical modelling of electrical machines from The University of Nottingham, Nottingham, U.K., in 2005. He subsequently worked as a Researcher with The University of Nottingham on high-performance electrical drives and on the design and modelling of electromagnetic actuators for aerospace applications. Since 2006, he has been the Project Manager of the GE Aviation Strategic Partnership. In 2008, he was appointed as a Lecturer in electrical machines; in 2011, as an Associate Professor; and in 2013, as a Professor at The University of Nottingham. His main research interests include the design and modelling of high-performance electric drives and machines. Prof. Gerada serves as an Associate Editor for the IEEE TRANSACTIONS ON INDUSTRY APPLICATIONS and is the past Chair of the IEEE IES Electrical Machines Committee.

G. Valente received the Master degree (Hons.) in Electrical Engineering in 2014 both from the University of Padova, Italy and the Ph.D. degree in electrical machines design and control from the University of Nottingham, UK in 2018. He is now working as a Research Fellow with the Power Electronics, Machines and Control Group, University of Nottingham, UK. His research interests include bearingless machines, high speed machines, traction machines and multiphysics-based optimization of electrical machines.